Performance Evaluation of Deception Against Synthetic Aperture Radar Based on Multifeature Fusion

Tian Tian, Feng Zhou, *Member, IEEE*, Yuchen Li, Bin Sun, Weiwei Fan, Chen Gong, *Senior Member, IEEE*, and Shuang Yang

***Abstract*—Deception is an effective means of jamming against synthetic aperture radar (SAR). The performance of deceptive jamming is affected by the accuracy of parameter measurement and the applied antijamming methods of SAR. In this article, we analyze the accuracy of current deceptive jamming evaluation indicators, propose a new method for evaluating the performance of deceptive jamming based on the combination of typical dominant deceptive jamming evaluation indicators, and recessive indicators extracted by convolutional neural networks, and obtain a level of deceptive jamming using a softmax activation function in a fully connected network. Deceptive jamming images affected by the SAR motion parameter measurement error are taken as training and test sets. Finally, the moving and stationary target acquisition and recognition database is used as a deceptive jamming template in order to verify the effectiveness of the proposed method.**

***Index Terms*—Convolutional neural network (CNN), deceptive jamming, electronic countermeasure (ECM), synthetic aperture radar (SAR).**

I. Introduction

SYNTHETIC aperture radar (SAR) is widely used in military and civilian applications, such as target classification, identification, and detection due to its high resolution at all times of day and in all types of weather [1]. To protect targets or regions of interest from the malicious reconnaissance of SAR, research into jamming has been of great interest in electronic countermeasure (ECM) devices [2], [3]. Deception is one of the most important techniques in the SAR jamming. The performance evaluation of deceptive jamming (PEoDJ) against SAR is useful for testing, upgrading, and combatting ECM methods and equipment [4]–[8], although there have been relatively few studies of the PEoDJ.

SAR ECM is a dynamic game process with incomplete information [9]–[11]. With the development of intelligent systems such as adaptive radar, adaptive electronic warfare, and intelligent ECM, adaptive PEoDJ has become an indispensable component of the SAR closed-loop game system [12]–[14]. The PEoDJ is a prerequisite for resource scheduling and decision-making in intelligent ECM systems. Therefore, the study of the real-time PEoDJ with high accuracy and stability is of great importance.

The purpose of jamming is to hinder or destroy the information retrieval capability of SAR. The traditional rules for PEoDJ generally utilize the changes in SAR images before and after jamming. The proposed deceptive jamming evaluation criteria include the information criterion [15]–[17], power criterion [18], [19], and efficiency criterion [20].

In order to evaluate the performance of deceptive jamming, the imaging characteristics of SAR can simultaneously utilize three aspects of indicators: the data domain, such as the signal-to-jamming ratio, and information loss ratio [18]; the scatterer target domain, such as the integral sidelobe ratio, peak sidelobe ratio, and impulse response width [22], [23]; and the scene target domain, such as image mean, image variance, Euclidean distance [24], equivalent number of looks (ENL) [25], correlation coefficient [25]–[27], dynamic range, image entropy [28], [29], and structural similarity (SSIM) [30], [31].

Unfortunately, these indicators are limited in practical application because they only focus on the variation of a single image and cannot directly judge the performance of a jamming method. Furthermore, they cannot meet the real-time requirement of today's ECM devices. The jamming indicator is empirically selected as the evaluation criterion in deceptive jamming. These jamming indicators are of low universality for a series of deceptive jamming images. Qin *et al.* obtained a high level of SAR deceptive jamming by introducing weighted summation of various evaluation indicators, but could not guarantee the accuracy for a large number of samples [21], [32].

Manuscript received April 1, 2020; revised June 23, 2020, September 2, 2020, and September 20, 2020; accepted September 21, 2020. Date of publication October 5, 2020; date of current version January 6, 2021. This work was supported in part by the National Natural Science Foundation of China under Grant 61631019, Grant 61801347, Grant 61801344, Grant 61971332, and Grant 62001350; in part by the China Postdoctoral Science Foundation under Grant 2016M602775, Grant 2017M613076, and Grant 2020M673346; in part by Aeronautical Science Foundation of China under Grant 20180181003; in part by Joint Fund of Ministry of Education under Grant 6141A02022367; and in part by Natural Science Basic Research Plan in Shaanxi Province of China under Grant 2020JQ-312. *(Corresponding author: Feng Zhou.)*

Tian Tian, Feng Zhou, Yuchen Li, Weiwei Fan, and Shuang Yang are with the Ministry Key Laboratory of Electronic Information Countermeasure and Simulation, Xidian University, Xi'an 710071, China (e-mail: dtian_1992@163.com; fzhou@mail.xidian.edu.cn; yuchenli233333@gmail.com; fww1991xxy@163.com; yangsh_xidian@163.com).

Bin Sun is with the Jinzhou Test Research Center, Jinzhou 121000, China (e-mail: ben1017617@126.com).

Chen Gong is with the University of Science and Technology of China, Hefei 230026, China (e-mail: cgong821@ustc.edu.cn).

Digital Object Identifier 10.1109/JSTARS.2020.3028858

With continuous growth of computation power, research on deep learning has increased. Convolutional neural networks (CNNs) have been applied in many fields, such as speech recognition and optical image recognition [34]–[37], to obtain image texture information and capture the spatial features between pixels. CNNs have also been effective in the classification and recognition of radar targets. This article proposes a new performance evaluation method for the deceptive jamming based on the combination of typical deceptive jamming evaluation indicators and recessive indicators extracted by CNNs. We attain the performance evaluation result through the use of the softmax activation function in fully connected networks. The proposed method can improve the adaptive and real-time processing capabilities of the PEoDJ and resolve the issues of poor universality and weak real-time assessment capability. At the same time, we analyze the influence of the measurement error of the SAR platform motion parameter on a deceptive jamming image. By adding velocity and position measurement error, different levels of deceptive jamming samples are generated [38]. This solves the problem of a limited number of deceptive jamming samples.

The remainder of this article is organized as follows. Section II introduces the dominant deceptive jamming indicators, which have clear physical meaning, and recessive indicators extracted according to the CNN. We focus on the dominant and recessive indicators as input to a fully connected network and obtain deceptive jamming levels through classifiers. Section III analyzes the influence of the SAR platform motion parameter measurement error on jamming performance. After adding velocity and position measurement errors, the training and test samples of deceptive images are generated. Section IV demonstrates the effectiveness of the proposed method using deceptive images, which are generated using the moving and stationary target acquisition and recognition (MSTAR) database as the original deceptive jamming template. Section V offers our conclusion.

II. Performance Evaluation Network Construction of Deceptive Jamming

In this section, we first introduce the physical meaning of PEoDJ indicators, which are known as dominant indicators, against SAR. We then introduce the recessive indicators extracted based on the CNN and concatenate them with the dominant indicators to form a new feature vector. Such results in the generation of the performance evaluation network of deceptive jamming. The proposed method can resolve the issues of traditional performance evaluation methods, such as subjectivity, poor generalization ability, and inability to meet the stringent real-time requirements of specific services. Compared with general multifeature weighting methods, the proposed method has higher confidence in setting weights.

A. Dominant Indicator Extraction Based on Traditional Methods

By comparing an ideal SAR imaging distribution and the imaging result generated by a deceptive jammer, the performance level of deception jamming is obtained [21]. For a single image, assume that the size of the deceptive jamming scene is $[N_r, N_a]$. Ideally, a SAR imaging result is represented by $R = \{r(x_i, y_j)\}$. When a SAR is jammed by a deceptive jammer, the imaging result is represented by $G = \{g(x_i, y_j)\}$, where the gray values of the two images on the scatterer (x_i, y_j) are $r(x_i, y_j)$ and $g(x_i, y_j)$, respectively. The means and variances of the two images are as follows:

$$\begin{cases} \mu_R = \frac{\sum_{i=1}^{N_r}\sum_{j=1}^{N_a} r(x_i,y_j)}{N_r N_a} \\ \sigma_R^2 = \frac{\sum_{i=1}^{N_r}\sum_{j=1}^{N_a} (r(x_i,y_j)-\mu_R)}{N_r N_a} \end{cases} \tag{1}$$

$$\begin{cases} \mu_G = \frac{\sum_{i=1}^{N_r}\sum_{j=1}^{N_a} g(x_i,y_j)}{N_r N_a} \\ \sigma_G^2 = \frac{\sum_{i=1}^{N_r}\sum_{j=1}^{N_a} (g(x_i,y_j)-\mu_G)}{N_r N_a}. \end{cases} \tag{2}$$

The Euclidean distance (d) compares the gray level at equivalent locations between the SAR image before and after deceptive jamming. After finding the square of the difference between $r(x_i, y_j)$ and $g(x_i, y_j)$, d is obtained as [24]

$$d = \sqrt{\sum_{i=1}^{N_r}\sum_{j=1}^{N_a} \left(r\left(x_i, y_j\right) - g\left(x_i, y_j\right)\right)^2}. \tag{3}$$

As the difference between the signals increases, d also increases. In the PEoDJ, a larger d between the real and false images leads to lower fidelity of the SAR deceptive jamming. Although the range of d is infinite, there is no upper bound of convergence. We can only analyze the jamming performance for the same scenario under different jamming conditions, but not for a single deceptive jamming image or group of different scenes.

Similar to the Euclidean distance, the mean square error (MSE) [33] measures the fidelity of deceptive jamming by

$$\mathrm{MSE} = \frac{1}{N_r N_a}\sum_{i=1}^{N_r}\sum_{j=1}^{N_a} \left(r\left(x_i, y_j\right) - g\left(x_i, y_j\right)\right)^2. \tag{4}$$

The MSE increases with the difference between the signals, hence a smaller MSE leads to better jamming performance.

The correlation coefficient (c) [25]–[27] characterizes the statistical correlation between two images, defined as

$$c = \frac{\sum_{i=1}^{N_r}\sum_{j=1}^{N_a} r\left(x_i, y_j\right) g\left(x_i, y_j\right)}{\sqrt{\sum_{i=1}^{N_r}\sum_{j=1}^{N_a} r^2\left(x_i, y_j\right)\sum_{i=1}^{N_r}\sum_{j=1}^{N_a} g^2\left(x_i, y_j\right)}}. \tag{5}$$

Since the gray value is nonnegative, i.e., $r(x_i, y_j) \geq 0$ and $g(x_i, y_j) \geq 0$, we can deduce that $0 < c \leq 1$, where a larger c indicates a stronger correlation between the false scene imaging result and the original scene. When c is close to 1, lower parameter measurement error is introduced in the deceptive jamming modulation.

SSIM evaluates the similarity between images by comparing the differences in image structure information [30], [31]. SSIM simulates the process of biological observation of objects based on the human visual system. It is expressed mathematically as

$$\mathrm{SSIM} = L\left(R, G\right) C\left(R, G\right) S\left(R, G\right) \tag{6}$$

where $L(R,G)$, $C(R,G)$, and $S(R,G)$ are the brightness comparison, contrast comparison, and structure comparison, respectively, which can be expressed as

$$L(R,G) = \frac{2\mu_R\mu_G + C_1}{\mu_R^2 + \mu_G^2 + C_1}$$
$$C(R,G) = \frac{2\sigma_R\sigma_G + C_2}{\sigma_R^2 + \sigma_G^2 + C_2}$$
$$S(R,G) = \frac{\sigma_{RG} + C_3}{\sigma_R\sigma_G + C_3} \tag{7}$$

where R and G denote the real SAR image and the generated deceptive jamming image, respectively; and C_1, C_2, and C_3 are specific small values included to prevent a zero denominator. Since SSIM addresses the correlation between local area pixel points, it is more sophisticated than simply calculating the pixel point parameters between images. A higher SSIM implies greater similarity of two images, and a more realistic deceptive jamming image.

The equivalent number of looks (ENL) [25] is commonly adopted to measure the speckle suppression of a single SAR image. It is defined as the ratio of the mean and variance of the image

$$\mathrm{ENL} = \frac{\mu}{\sigma^2}. \tag{8}$$

A larger ENL indicates that an image is well smoothed. By comparing the difference of the equivalent number of looks ($\Delta\mathrm{ENL}$) between a real SAR image R and a deceptive jamming image G, the performance of the deceptive jamming can be analyzed

$$\Delta\mathrm{ENL} = |\mathrm{ENL}_R - \mathrm{ENL}_G| \tag{9}$$

where $|\cdot|$ denotes the absolute value. The larger the $\Delta\mathrm{ENL}$, the better the performance of deceptive jamming is modulated.

Image entropy [28], [29] is defined as

$$H = -\sum_{i=0}^{L-1} P_i \log P_i \tag{10}$$

where L is the total number of gray levels and P_i is the probability of gray level i. Image entropy characterizes the aggregation of the gray distribution of an image. Richer information included in an image implies larger entropy. The degradation of deceptive jamming quality leads to information loss. Deceptive jamming performance can be evaluated by calculating the difference between the image entropy values of R and G

$$\Delta H = |H_R - H_G|. \tag{11}$$

Theoretically, all of the above indicators can be used to evaluate the quality of deceptive jamming. Each of them measures a different aspect of deceptive jamming, which, however, may lead to erroneous conclusions. Some of these indicators either have no boundaries or a very wide range. Therefore, we cannot judge the performance of deceptive jamming by their absolute values. Moreover, when using a multifeature weighted fusion method, the vast difference in the distribution intervals of these indicators exerts negative effects on the weight distribution, since the weights tend to be more advantageous for features with larger values. This will be verified in subsequent experiments.

B. Recessive Indicator Extraction Method Based on CNN

A CNN is a neural network designed to process data with similar grid structures [35], such as time series or image data. CNNs use a convolution operation instead of a general matrix multiplication operation in at least one layer. Unlike fully connected networks, CNNs use weight-sharing to reduce the number of network parameters and alleviate the problem of overfitting. AlexNet (2012) was a breakthrough in the effectiveness of a CNN for complex models [36]. Subsequently, researchers continued to explore CNNs and proposed more powerful CNN structural models. Since SAR deceptive jamming images consist of typical grid data, we can utilize CNNs to extract indicators for the PEoDJ.

A CNN includes an input layer, convolutional layers, pooling layers, and a final output layer. The convolutional layer is the core layer, and is used to extract image features. It has the characteristics of local perception and parameter sharing. Each neuron in the current layer extracts the same feature of all feature maps in the previous layer, so that the features between different neurons in each layer are independent. The operations of the convolutional layer include convolution and activation. In forward propagation, the convolutional kernel will slide on the width and high dimension of the input data, calculate the inner product of the entire convolutional kernel, and the input data at any position, generate a 2-D feature map, and overlay the activation maps of different filters in the depth direction to generate the output data. Define the input of the previous layer as $I_i^{(l-1)}(i = 1, \ldots, N_{l-1})$, where N_{l-1} is the number of feature units of the $(l-1)\,\mathrm{th}$ layer, and the output is $I_j^{(l)}(j = 1, \ldots, N_l)$, where N_l is the number of feature units of the $l\mathrm{th}$ layer. Convolutional processing can be expressed as

$$O_j^{(l)}(x,y) = \sum_{i=0}^{N_{l-1}} \sum_{u,v=0}^{F-1} k_{ji}^{(l)}(u,v) \cdot I_i^{(l-1)}(x-u, y-v) + b_j^l \tag{12}$$

where $I_i^{(l-1)}(x,y)$ is the activation value of the $i\mathrm{th}$ unit at (x,y) of the $(l-1)\mathrm{th}$ layer, $I_j^{(l)}(x,y)$ is the activation value of the *j*th unit at $(x,y)$of the $l\mathrm{th}$ layer, $k_{ji}^{(l)}(u,v)$ is the weight of the $i\mathrm{th}$ unit at the $(l-1)\mathrm{th}$ layer and the *j*th unit at the $l\mathrm{th}$ layer, and $b_j^{(l)}$ is the bias of the *j*th unit at the $l\mathrm{th}$ layer. The activation value of the *j*th unit in the *l*th layer can be expressed as

$$I_j^{(l)}(x,y) = f\left(O_j^{(l)}(x,y)\right) \tag{13}$$

where $f(x)$ is the rectified linear unit (ReLU). The ReLU layer is used to activate the data after every convolution in order to increase the nonlinear characteristics of the network and provide the model with stronger classification expression ability.

When mapped to a higher-dimensional space, the final decision surface is decomposed into multiple planes. As the neural network deepens, multiple piecewise planes are required to fit the final decision surface and achieve nonlinear classification.

The convolutional kernels and biases are the parameters that must be trained.

The pooling layer is added after the convolutional layer. Its function is to reduce the data dimensions and semantically fuse similar features, such that the model can extract a wider range of features. The pooling layer can also reduce the amount of calculation and the number of required parameters, leading to the characteristic of feature invariance.

In most cases, the maximum and average pooling independently operate on each depth slice of input data in the pooling layer. Such types of pooling can change the spatial size of data. In this article, we choose maximize pooling with step size 2, which returns the maximum value in the pooling window. The image features are extracted after multiple convolution and pooling operations.

The softmax activation layer is the last layer of the entire network, whose primary purpose is to complete the classification task. The output layer of the CNN is a K-dimensional vector whose elements correspond to the posterior probability $p_i = P(y = i|I^{(L)}), i = 1, \cdots, K$ of each class. $I^{(L)}$ is the input of the softmax layer, which is obtained by the weighted sum of the previous fully connected layer. The actions of softmax can be expressed as

$$p_i = \frac{\exp\left(I_i^{(L)}\right)}{\sum_{j=1}^{K} \exp\left(I_j^{(L)}\right)} \tag{14}$$

where $I_i^{(L)}$ is the weighted sum of the *i*th node of the last fully connected layer and L is the number of layers.

Given a training set with m samples, which can be expressed as $\{(x^{(i)}, y^{(i)}), i = 1, \cdots, m\}$, $y^{(i)}$ is the real label of the target, and the cross-entropy loss function can be defined as

$$L(\mathbf{k}, \mathbf{b}) = -\frac{1}{m} \sum_{i=1}^{m} \log P\left(y^{(i)} \middle| x^{(i)}; \mathbf{k}, \mathbf{b}\right) \tag{15}$$

where $\mathbf{k}$ and $\mathbf{b}$ are the weight and bias sets, respectively, of all the layers in the CNN.

By minimizing the cross-entropy loss function, the weight $\mathbf{k}$ will be updated to increase the probability of the correct category, which is equivalent to maximum likelihood estimation. The goal of softmax is not to minimize the square of the error, but to minimize the cross entropy of the known distribution and the probability distribution of the network estimation in order to obtain better classification results.

The weight and bias are updated by minimizing the loss function. Due to the complexity of the global loss function, it is unrealistic to directly calculate and analyze the global minimum loss function, although it is feasible in practice to solve for the partial derivative of the corresponding parameter. Therefore, the loss function can be minimized by iterative optimization, and the simplest way to do so is by gradient descent.

In a CNN, the weight parameter update of the loss function can be realized by back propagation, in which random gradient descent is used to optimize the network parameters. To update the network parameters, the residual $\delta_i^l (i = 1, \ldots, N_l)$ of the intermediate variable must first be calculated, which is realized by calculating the partial derivative of the corresponding weight parameters for each cell. For the elements of the output layer, the residual can be expressed as

$$\delta_i^l = -\left(y^{(i)} - p_i\right) \tag{16}$$

where p_i is the predicted value of the CNN. The residual of the front layer can then be calculated according to the residual of the output layer. If the $(l+1)\text{th}$ layer is the convolutional layer, the residual of the *l*th layer can be expressed as

$$\delta_i^l(x, y) = \sum_j \sum_{u,v=0}^{F-1} k_{ji}^{(l+1)}(u, v) \cdot \delta_j^{(l+1)}(x + u, y + v) \tag{17}$$

where $k_{ji}^{(l+1)}$ is the weight connecting the *i*th unit at the *l*th layer and the *j*th unit at the $(l+1)\text{th}$ layer, and $\delta_j^{(l+1)}$ is the residual of the *j*th unit at the $(l+1)\text{th}$ layer. Although there is no trainable weight parameter in the pooling layer, the residual must be transferred back to the low-level network. If the $(l+1)\text{th}$ layer is the maximum pooling layer, the residual of the *l*th layer can be expressed as

$$\begin{aligned}\delta_i^l(x, y) = f'\left(I_i^{(l)}(x, y)\right) \cdot \sum_{m,n} \delta_i^{(l+1)}(m, n) \\ \cdot \varepsilon\left(u_{i,m} + ms - x, v_{i,n} + ns - y\right)\end{aligned} \tag{18}$$

where $f'(x)$ is the derivative of the nonlinear excitation function, which in this article is ReLU.

By calculating the residuals of each layer, the gradients of the weight and the bias of each layer can be calculated as

$$\frac{\partial L}{\partial k_{ji}^{(l)}(u, v)} = \sum_{x,y} \delta_j^{(l)}(x, y) \cdot I_j^{(l-1)}(x - u, y - v) \tag{19}$$

$$\frac{\partial L}{\partial b_{ji}^{(l)}} = \sum_{x,y} \delta_j^{(l)}(x, y). \tag{20}$$

Using gradient descent to update the weight and bias of the network, through forward propagation and back propagation, the network finally converges, stable network parameters are obtained, and the SAR recessive features of deceptive jamming images are extracted.

Fig. 1 shows the CNN structure adopted in this article. It includes six convolutional layers, three max pooling layers, two fully connected layers, and one softmax classifier. Smaller convolution kernels usually have a better feature extraction effect and higher recognition result [39]. Therefore, we chose a 3×3 convolutional kernel, which can achieve a good balance between reducing the number of parameters and effectively extracting image features. The parameters in the convolutional kernel are obtained through training, and its learnable parameters through a supervised learning method with a training set. There are eight 3×3 convolutional kernels in the first and second convolutional layers, 16 3×3 convolutional kernels in the third and fourth convolutional layers, and 32 3×3 convolutional kernels in the fifth and sixth convolutional layers. The stride size and padding of a convolutional kernel are both 1. With the deepening of a convolutional layer, the features of the feature map become increasingly abstract and more difficult to extract. It is generally

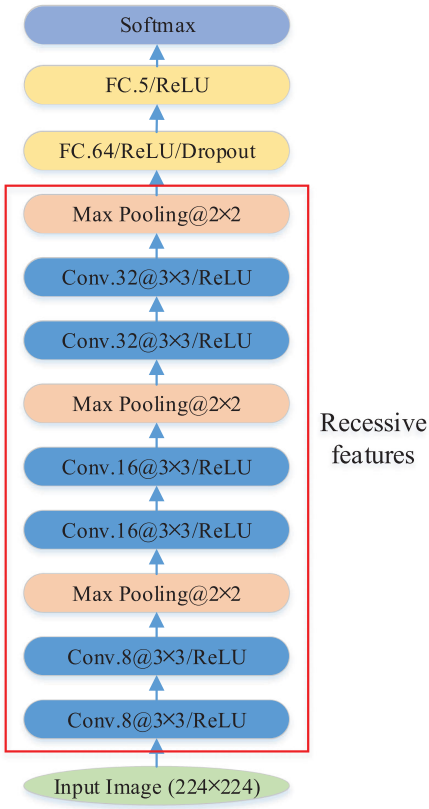

Fig. 1. Applied CNN structure.

necessary to increase the depth of a convolutional kernel to fully describe the in-depth features with more parameters [40]. After every two convolutional layers, a max pooling layer with pooling size 2×2 and stride size 2 is added. Dropout is added to the first fully connected layer with probability $p = 0.5$. After three sets of convolution and pooling operations, 32 feature maps of size 28×28 are obtained. The first fully connected layer has 64 nodes, and the second has five nodes, followed by the softmax activation function for classification. The input data consists of a single-channel grayscale image of size 224×224. The batch size is 64 and the learning rate is 10^{-4}. During the input of the recessive part, the mean value of the deceptive jamming image is subtracted in order to make the overall mean value of the image zero, which is conducive to CNN training, thus enabling the network to more easily converge while avoiding gradient explosion.

C. Dominant and Recessive Feature Joint Weight Construction

To integrate multiple image quality indicators, the traditional method often applies weighted summation [21]

$$y = \sum_i k_i x_i + b \tag{21}$$

where x_i is the ith performance evaluation indicator of the SAR deceptive jamming image; k_i is the corresponding weight; b is a bias; $f(\cdot)$ is a nonlinear activation function; and y is the comprehensive result.

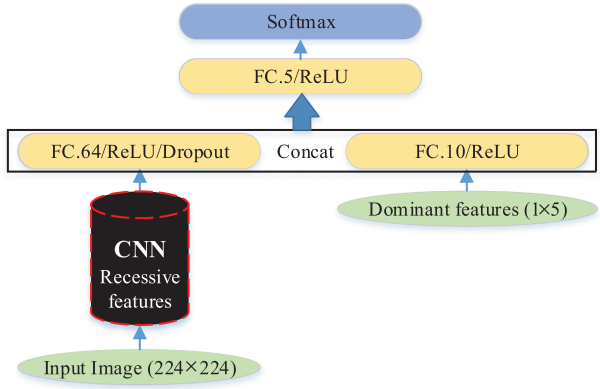

Fig. 2. Proposed performance evaluation network of deceptive jamming.

Weighted summation is essentially a linear model that can be represented by a perceptron [41], [42], which can only solve the linear separable problem. Due to the complexity of the performance evaluation of deceptive jamming, the weighted summation model must be extended to a nonlinear version. Fig. 2 shows the proposed performance evaluation network framework of deceptive jamming, from which both recessive and dominant indicators can be obtained. The recessive indicators are extracted according to the CNN, whose structure is described in the red box in Fig. 1. The dominant indicators are determined according to the classical image assessment indicators. To avoid the situation in which the sensitivity of the weight to the parameter is large, the dominant feature is linearly normalized to $[0, 1]$:

$$x_{nor} = \frac{x - x_{\min}}{x_{\max} - x_{\min}} \tag{22}$$

where x_{nor} is the normalized dominant feature, x is the original dominant feature, and $x_{\max}$ and $x_{\min}$ are the respective maximal and minimal values in the original feature set. These dominant features are combined to form the new feature map.

In Fig. 2, the first fully connected layer has 64 nodes that are extracted from recessive features and the second has 10 nodes from dominant features separately. The third fully connected layer has five nodes, followed by the softmax activation function for classification. The framework is end-to-end, and the weights are automatically learned from deceptive jamming samples. In our experiment, the weights obtained by training are fixed. Finally, the levels of deceptive jamming are obtained.

III. Generation Of Deceptive Jamming Samples

Deceptive jamming modulation is achieved based on digital radio frequency memory, which consists of amplitude-, delay-, and phase-modulation terms [38]. A jamming signal intercepted by a deceptive jammer is the signal directly transmitted by SAR, which contains the error of the SAR hardware system and the motion error information of its platform. Hence, it has the same time sequence and waveform characteristics as the signal transmitted by SAR. Because of this, it can produce realistic false targets.

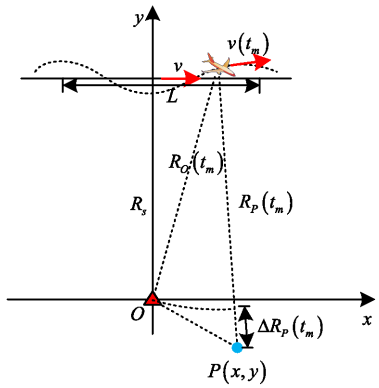

Fig. 3. Geometry of deceptive jamming against SAR.

Owing to the limit in reconnaissance accuracy of the jammer, the geometric parameters used for deceptive jamming modulation have difficulty accurately containing the motion error of the SAR platform. Thus, the jamming signal may not completely match the real echo. As a result, the parameter measurement error in the processing of echo motion compensation is either inaccurate or has difficulty estimating the real scene. The unified compensation with the false scene results in defocusing of the false or real scene, which diminishes the performance of deceptive jamming. Therefore, deceptive jamming samples with different levels can be generated by adding different SAR parameter measurement errors. We analyzed the influence of parameter measurement on the performance of deceptive jamming.

A. Analysis of Factors Affecting Performance of Deceptive Jamming

The imaging geometry of a point target can be characterized by the ideal stop-and-go model, as shown in Fig. 3. In a Cartesian coordinate system, the x-axis is the azimuth dimension and is parallel to the flight direction of the SAR platform. The y-axis is the range dimension in the oblique plane and is perpendicular to the x-axis. The origin O is the pointing position of the beam center at the initial time at the jammer's location. $P(x, y)$is the location of an arbitrary false scatterer and L is a synthetic aperture length. Ideally, SAR flies along a straight line with velocity v. R_s is the shortest range between a SAR platform and a jammer, and is ideally a constant. When affected by external factors such as clouds and air flow, as well as the navigation capability of a radar platform, the real SAR trajectory is a curve, as depicted by the dotted line. Thus, there is some deviation of R_s in every slow time t_m, which is expressed as $R_s(t_m)$. The instantaneous slant range between the SAR and jammer is

$$R_O\left(t_m\right)=\sqrt{R_s^2\left(t_m\right)+v^2\left(t_m\right)t_m^2} \tag{23}$$

where t_m is the slow time.

The theoretical instantaneous slant range between the SAR and a false scatterer $P(x, y)$ is

$$R_P\left(t_m\right)=\sqrt{\left(R_s\left(t_m\right)+y\right)^2+\left(x-v\left(t_m\right)t_m\right)^2}. \tag{24}$$

The ideal Doppler frequency rate with scatterer $P(x, y)$ is

$$\gamma_a=\frac{v^2\left(t_m\right)}{2\left(R_s\left(t_m\right)+y\right)}. \tag{25}$$

Comparing (23) and (24), the difference of slant range between real and false scatterers is

$$\Delta R_P\left(t_m\right)=R_P\left(t_m\right)-R_O\left(t_m\right). \tag{26}$$

For computational convenience, we approximate the delay term in (26) as a second-order Taylor series of t_m

$$\begin{aligned}\Delta R_P\left(t_m\right)&=y+\frac{x^2}{2\left(R_s\left(t_m\right)+y\right)}-\frac{xv\left(t_m\right)t_m}{\left(R_s\left(t_m\right)+y\right)}\\&\quad+\frac{\left[v\left(t_m\right)\right]^2t_m^2}{2}\left(\frac{1}{\left(R_s\left(t_m\right)+y\right)}-\frac{1}{R_s\left(t_m\right)}\right)\\&=r_0+r_1t_m+r_2t_m^2\end{aligned} \tag{27}$$

where

$$\begin{aligned}r_0&=y+\frac{x^2}{2\left(R_s\left(t_m\right)+y\right)}\\r_1&=-\frac{xv\left(t_m\right)}{\left(R_s\left(t_m\right)+y\right)}\\r_2&=\frac{v^2\left(t_m\right)}{2}\left(\frac{1}{\left(R_s\left(t_m\right)+y\right)}-\frac{1}{R_s\left(t_m\right)}\right)\end{aligned} \tag{28}$$

where r_0 is a constant term of t_m, whose value determines the position of a false scatterer in range; r_1 is a first-order term of t_m, whose value determines the imaging position of a false scatterer in the azimuth; and r_2 is a second-order term of t_m, whose value is related to the Doppler frequency rate.

When SAR platform trajectory deviation occurs, the instantaneous slant distance$R_s(t_m)$ and velocity $v(t_m)$ vary with t_m. Unfortunately, the precise measurement of the SAR motion parameter is not easy, although a key step in deceptive jamming is the accurate calculation of the difference of instantaneous slant range $\Delta R_P(t_m)$. This will affect the deceptive jamming quality.

1) Influence of $R_s(t_m)$ Measurement Error on Deceptive Jamming: The measurement error of $R_s(t_m)$ will affect all terms in (27). The errors in r_0 and r_1 caused by the $R_s(t_m)$ measurement error will result in offsets of the false scatterer image in range and azimuth, respectively. The r_2 error will lead to the mismatch of the false scatterer's signal to the corresponding match-filter function, causing the deceptive jamming image to be defocused, thus significantly degrading the deceptive jamming performance. In summary, the errors in r_0 and r_1 will cause the position of the false scatterer imaging to deviate from the preset coordinates, which will cause the distortion of the false scene. The deceptive jamming performance, however, will not change significantly. In contrast, r_2 error will cause obvious false scene defocusing, which will lead to the degradation of deceptive jamming.

Define the $R_s(t_m)$ measurement error as

$$\Delta R_s=\frac{\sum_{t_m=1}^{N_a}\left|R_s\left(t_m\right)-R_s\right|}{N_aR_s} \tag{29}$$

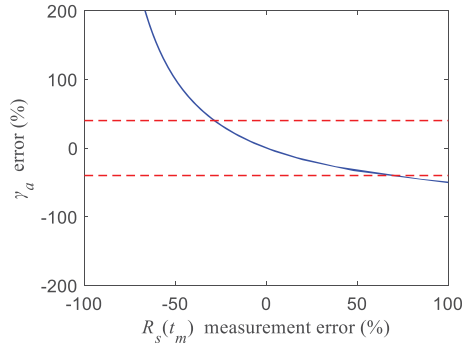

Fig. 4. Variation of Doppler frequency rate error with $R_s(t_m)$ measurement error.

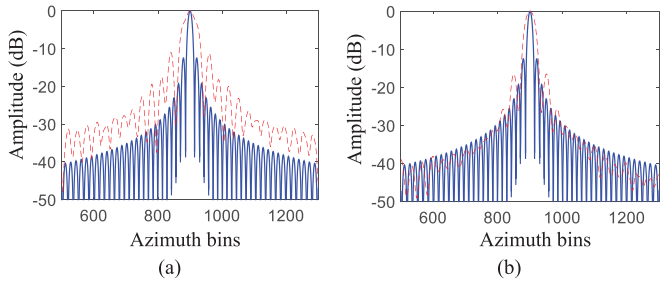

Fig. 5. Comparison of azimuth profiles of deceptive jamming scatterer with $\pm 20\%$ of $R_s(t_m)$ measurement error and real scatterer: (a) -20% of $R_s(t_m)$ measurement error; (b) 20% of $R_s(t_m)$ measurement error.

where $\Delta R_s \in (-1, 1)$. The corresponding Doppler frequency rate of a deceptive jamming signal after phase compensation is

$$\hat{\gamma}_a = \frac{v^2(t_m)}{2\left((1+\Delta R_s)\cdot R_s(t_m) + y\right)}. \tag{30}$$

The resulting Doppler frequency rate error is defined as

$$Dop_r = \frac{\hat{\gamma}_a - \gamma_a}{\gamma_a} = \frac{-\Delta R_s \cdot R_s(t_m)}{(1+\Delta R_s)\cdot R_s(t_m) + y}. \tag{31}$$

The variation of γ_a error caused by the $R_s(t_m)$ measurement error is plotted in Fig. 4. In the most extreme case, the $R_s(t_m)$ measurement error increases from -100% to 100%. Correspondingly, γ_a error decreases from $+\infty$ to 0, and then to approximately -50%. The physical meaning of -100% γ_a error is that r_2 is zero, i.e., no compensation is made for γ_a spatial-variability caused by deceptive jamming. The 100% γ_a error means that γ_a spatial-variability is compensated for twice.

There is no such extreme situation in reality. $R_s(t_m)$ measurement error is generally hundreds to thousands of meters. Fig. 5 compares the azimuth profile of deceptive jamming data with -20% or 20% of $R_s(t_m)$ measurement error and the real echo. The solid line represents the real echo, and the dotted line represents the false scatterer. Such result indicates that when the measurement error is -20% of $R_s(t_m)$, the performance of deceptive jamming becomes worse. The result is consistent with the curve plotted in Fig. 4.

2) Influence of $v(t_m)$ Measurement Error on Deceptive Jamming: Inevitable measurement errors in $v(t_m)$ similarly occur. The analysis of $v(t_m)$ measurement error is also discussed according to its effect on r_0, r_1, and r_2. Based on (27) and (28), $v(t_m)$ measurement error does not affect the position of the false scatterer in the range. The r_1 error caused by $v(t_m)$ measurement error will result in the offset of false scatterer images in the azimuth, but will not defocus them. $v(t_m)$ measurement error in r_2 will lead to γ_a error. This will result in the false scatterer's signal mismatch with the corresponding match-filter function, causing the deceptive jamming image to be defocused, thereby degrading the performance of deceptive jamming.

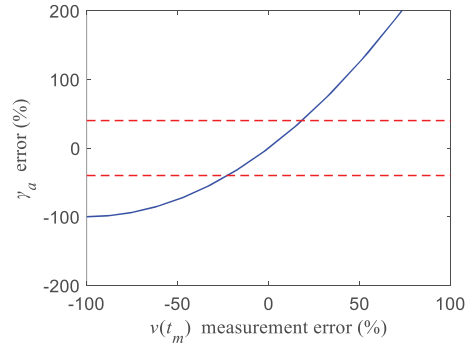

Fig. 6. Variation of Doppler frequency rate error with $v(t_m)$ measurement error.

Define $v(t_m)$ measurement error as

$$\Delta v = \frac{\sum_{t_m=1}^{N_a} |v(t_m) - v|}{N_a v} \tag{32}$$

where $\Delta v \in (-1, 1)$. The corresponding γ_a of a deceptive jamming signal after phase compensation is

$$\hat{\gamma}_a = \frac{(1+\Delta v)\cdot v^2(t_m)}{2\left(R_s(t_m) + y\right)}. \tag{33}$$

The resulting γ_a error is defined as

$$D_r = \frac{\hat{\gamma}_a - \gamma_a}{\gamma_a} = (\Delta v)^2 + 2\Delta v. \tag{34}$$

With the variation of the measurement error of $v(t_m)$, γ_a error compensated by a deceptive jamming signal is shown in Fig. 6. When $v(t_m)$ measurement error increases from -100% to 100%, the corresponding γ_a error varies from -100% to 0%, and continues to increase. Its physical meaning is the same as that caused by $R_s(t_m)$.

The $v(t_m)$ measurement error will not reach $\pm 100\%$ in reality. Therefore, we compare the image of the deceptive jamming data with -20% or 20% of $v(t_m)$ measurement error and the real echo. The azimuth profile is plotted in Fig. 7. The solid and dotted lines are the azimuth profiles of the real and false scatterers, respectively. This indicates that with a -20% $v(t_m)$ measurement error, the performance of deceptive jamming is better than the case with 20%. Such result is consistent with the curve plotted in Fig. 6.

B. Construction of Deceptive Jamming Samples Based on Measurement Error of SAR Motion Parameters

A deceptive jamming signal may be caused by the superposition of multiple false scatterers. The measurement error of

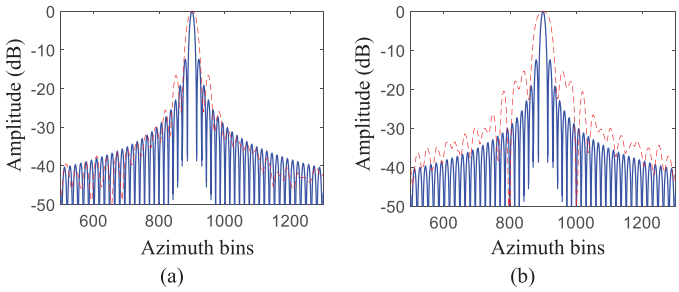

Fig. 7. Comparison of azimuth profiles of deceptive jamming scatterer with $\pm 20\%$ of $v(t_m)$ measurement error and real scatterer: (a) -20% of $v(t_m)$ measurement error; (b) 20% of $v(t_m)$ measurement error.

TABLE I
SAR SYSTEM PARAMETERS

Parameter	Value
Carrier frequency (f_0)	9.6 GHz
Bandwidth (B)	180 MHz
Pulse width (T_p)	2 *us*
Altitude (H)	7.5 km
Shortest range (R_s)	15 km
Squint angle (θ)	0°
Velocity (v)	110 m/s

the SAR motion parameter will lead to both position offset and defocusing of the entire jamming image. This will reduce the 2-D coherent accumulation gain of the jamming image. Therefore, the samples required for the deceptive jamming evaluation can be generated by the inaccurate measurement of the SAR motion parameters. After adding $R_s(t_m)$ and $v(t_m)$ measurement errors, the training and test samples for the PEoDJ are generated.

To visually depict the influence of $R_s(t_m)$ and $v(t_m)$ measurement errors on the imaging of a false target, experiments were carried out, as discussed in the following section, with the parameters listed in Table I. We used the MSTAR open dataset as the template for deceptive jamming. Random measurement error with variances 0.5%, 1.5%, 3%, 7%, and 12% were added to $R_s(t_m)$. The deceptive jamming images are presented in Fig. 8. When the error is small, the image edge defocuses, but not to an obvious extent. As $R_s(t_m)$ measurement error increases, the image position shifts in both range and azimuth, and the image quality degrades. More serious image defocusing leads to worse deceptive jamming quality.

IV. EXPERIMENTAL RESULTS

We evaluated the proposed method based on the data generated in Section III. The sizes of the training and testing datasets are listed in Table II. We utilized BMP-2 as the deceptive jamming template to generate the training and test sets, which were provided at 17° and 15° depression angles, respectively, under $R_s(t_m)$ measurement error with variances 0.5%, 1.5%, 3%, 7%, and 12%.

The applicable scope and limitations of current SAR deceptive jamming evaluation indicators were analyzed on specific samples. For a single deceptive jamming template, different

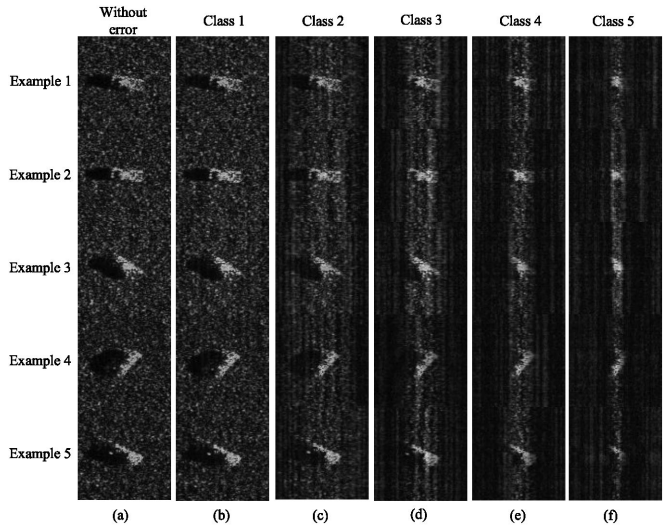

Fig. 8. False target imaging results under random $R_s(t_m)$ measurement error. (a) False scene imaging result without measurement error. False scene imaging result under $R_s(t_m)$ measurement error with variance of: (b) 0.5%; (c) 1.5%; (d) 3%; (e) 7%; (f) 12%.

TABLE II
DESCRIPTION OF TRAINING AND TEST SETS

Level	Training set	Test set
0.5%	698	587
1.5%	698	587
3.0%	698	587
7.0%	698	587
12.0%	698	587

$R_s(t_m)$ measurement errors were added to generate deceptive jamming images. The corresponding variation of these indicators in Section II-A is plotted in Fig. 9. The horizontal axis represents the added $R_s(t_m)$ measurement error, the vertical axis represents the corresponding indicators, the points comprise the simulation result of the image quality indicators corresponding to the measurement error, and the solid line is the fitting curve of the data.

From Fig. 9, we see that d and MSE increase with $R_s(t_m)$ measurement error, indicating that the performance of deceptive jamming images worsens. In addition, c decreases gradually, which indicates that the statistical correlation of the deceptive jamming image will decrease gradually due to $R_s(t_m)$ measurement error. SSIM decreases with increasing measurement error, which indicates the difference between the deceptive jamming image and the real one, and reflects the influence of $R_s(t_m)$ measurement error on the performance of deceptive jamming. ΔENL varies randomly with $R_s(t_m)$ measurement error, which cannot reflect the influence of parameter measurement error on the performance of deceptive jamming because the influence of $R_s(t_m)$ measurement error on the deceptive jamming image is mainly reflected in the position offset and defocus of the scatterer far from the jammer. The image center still maintains a high focusing energy. Its mean and variance are greatly affected by random noise, and cannot reflect the variation

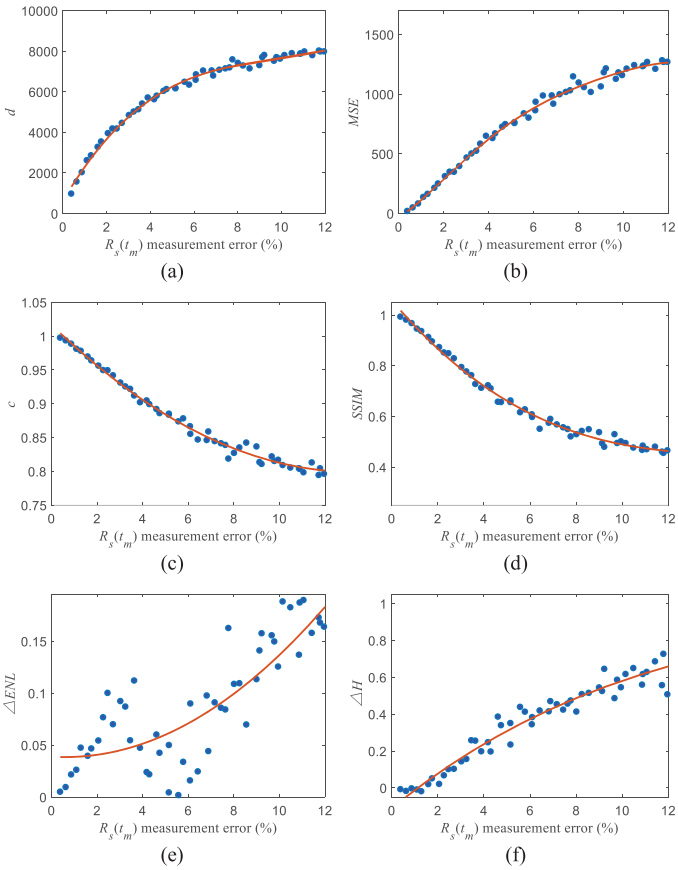

Fig. 9. Variations in dominant indicators of a single deceptive jamming image with $R_s(t_m)$ measurement error: (a) Euclidean distance (d). (b) Mean square error (MSE). (c) Correlation coefficient (c). (d) Structural similarity ($SSIM$). (e) Differential equivalent number of looks (ΔENL). (f) Difference between image entropy of $R$and G (ΔH).

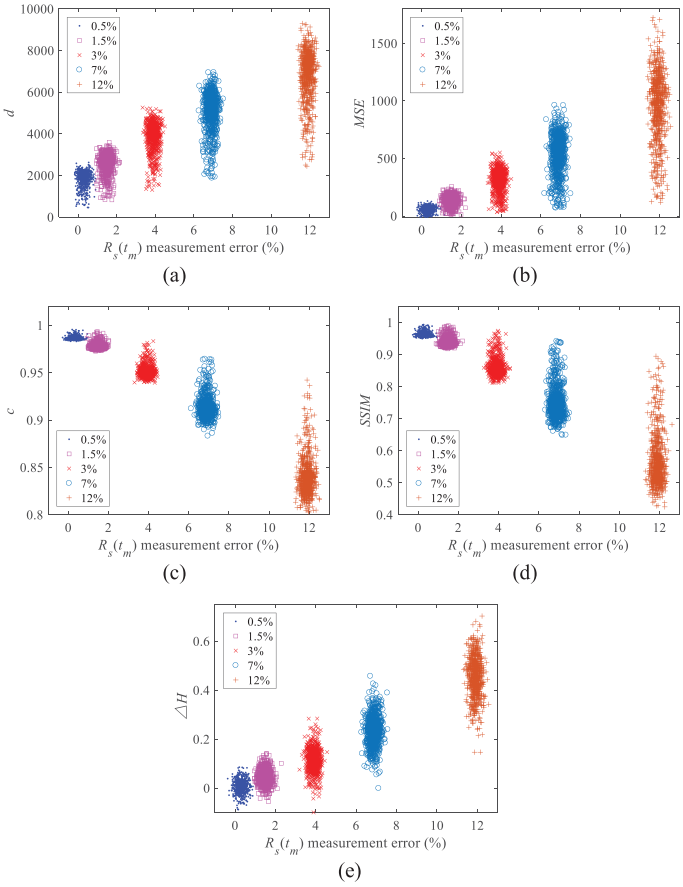

Fig. 10. Distribution of dominant indicators of training set with $R_s(t_m)$ measurement error. (a) Euclidean distance (d). (b) Mean square error (MSE). (c) Correlation coefficient (c). (d) Structural similarity (SSIM). (e) Difference between image entropy of $R$and G (ΔH).

of $R_s(t_m)$ measurement error. ΔH generally increases with $R_s(t_m)$ measurement error, which indicates that the deceptive jamming image information is lost as $R_s(t_m)$ measurement error increases. When $R_s(t_m)$ measurement error is large, the image entropy is affected by random noise, although it still reflects the influence of deceptive jamming.

According to Fig. 9, ΔENL is not a suitable evaluation criterion for the deceptive jamming. The trends of the remaining indicators are similar to a logarithmic distribution. As the measurement error increases, the deceptive jamming image deterioration decreases. This is why we apply the nonuniform error variation interval. The levels of deceptive jamming can be well discriminated, which is basically consistent with the theoretical analysis. Therefore, we selected d, MSE, c, SSIM, and ΔH as the dominant indicators in this article, and used them to evaluate the performance of deceptive jamming from different perspectives.

For a single sample, the trend of the indicator value is obvious after adding different $R_s(t_m)$ measurement errors. Multiple deceptive jamming samples, however, belong to one level, whose range of indicators is relatively large. The distribution of indicators for the five levels of training samples is shown in Fig. 10.

After adding the $R_s(t_m)$ measurement error, the indicators of different levels of deceptive jamming images overlap to some extent. Fortunately, there is still a general increasing or decreasing trend. To divide the range of each image quality indicator, we plot the histograms of different levels of samples under different indicators along with their corresponding fitted probability distributions in Fig. 11.

The performance of deceptive jamming images under different $R_s(t_m)$ measurement errors obviously differs. Based on the fitting results of each indicator after repeated experiments, the error interval of each indicator was divided by the minimum error rate criterion. The classification boundaries for different levels of the deceptive jamming images are listed in Table III.

Based on Table III, the performance of 2935 deceptive jamming images in the test set are evaluated, with the confusion matrix with dominant indicators presented in Table IV, while each row in Table IV represents a level of deceptive jamming samples that is evaluated in the test set. Each column represents the true level of jamming samples. The accuracy is defined as

$$acc\,(f;D)=\frac{1}{m}\sum_{i=1}^{m}I\left(f\left(x^{(i)}\right)=y^{(i)}\right) \tag{35}$$

where $D=\{(x^{(1)},y^{(1)}),(x^{(2)},y^{(2)}),\cdots,(x^{(m)},y^{(m)})\}$ is the test set; $y^{(i)}$ is the true label of jamming sample $x^{(i)}$; and $I(\cdot)$ is a mapping function that equals 1 if $f(x^{(i)})=y^{(i)}$, and 0 otherwise.

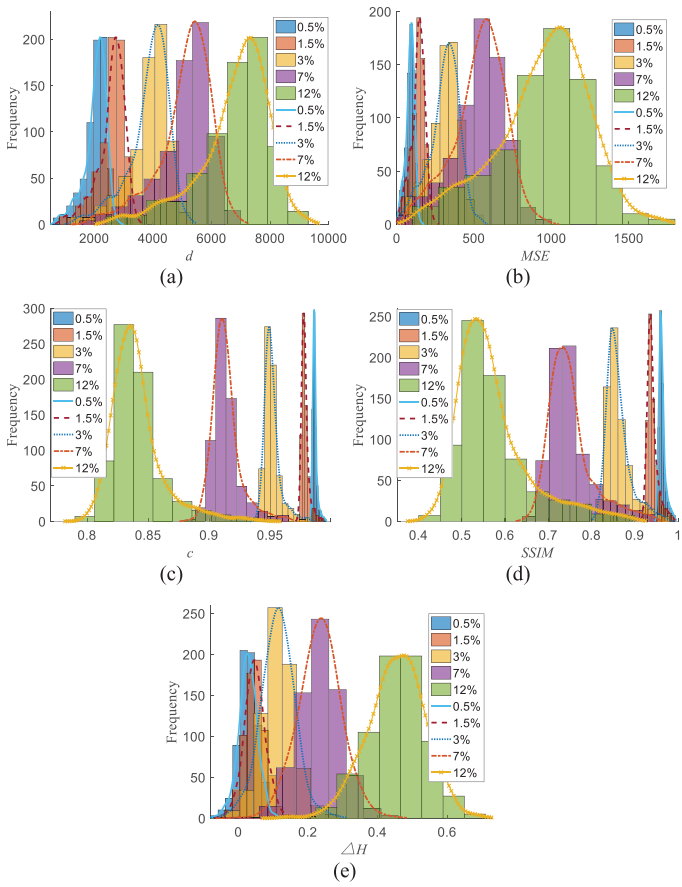

Fig. 11. Histogram of dominant index of training set with $R_S(t_m)$ measurement error. (a) Euclidean distance (d). (b) Mean square error (MSE). (c) Correlation coefficient (c). (d) Structural similarity (SSIM). (e) Difference between image entropy of R and G (ΔH).

TABLE III
CLASSIFICATION BOUNDARIES OF DIFFERENT PERFORMANCES OF DECEPTIVE JAMMING IMAGES

$R_s(t_m)$ measurement error / Indicators	0.5%	1.5%	3%	7%	12%
d	<2000	2000-3100	3100-4600	4600-6100	>6100
MSE	<110	110-175	175–410	410–740	>740
c	>0.98	0.97–0.98	0.94–0.97	0.89–0.94	<0.89
SSIM	>0.95	0.92–0.95	0.81–0.92	0.67–0.81	<0.67
ΔH	<0.035	0.035–0.065	0.065–0.17	0.17–0.33	>0.33

The correlation coefficient and structural similarity exhibit good discrimination to different levels of deceptive jamming images. The MSE and Euclidean distance display high evaluation precision when the $R_s(t_m)$ measurement error is small, but show a poor distinction between levels when the

$R_s(t_m)$ measurement error is large, because the histogram has some overlap between levels. In contrast, the evaluation precision of differential image entropy values varies in the opposite manner. Table IV indicates that a single image quality indicator is not enough to characterize the performance of a set of deceptive images. Fortunately, the accuracy rate of all the indicators is more than 50% at all levels. Therefore, these indicators have value as performance evaluation features of deceptive jamming.

In Table V, dominant indicators are used as weak classifiers, and the voting weighted method is employed as the integrated classifier to recognize the five jamming levels [21]. The test results reveal that the accuracy of this approach is much worse than that of the optimal indicator. Also, some rejected samples must be evaluated.

TABLE IV
CONFUSION MATRIX OF DECEPTIVE JAMMING EVALUATION RESULTS WITH DOMINANT INDICATORS

	d					
	0.5%	1.5%	4%	7%	12%	**Accuracy**
0.5%	**561**	26	0	0	0	95.57%
1.5%	257	**325**	5	0	0	55.37 %
4%	43	85	**445**	14	0	75.81 %
7%	13	27	161	**378**	8	64.40 %
12%	1	12	40	143	**391**	66.61 %
Average						**71.55%**
	MSE					
	0.5%	1.5%	4%	7%	12%	**Accuracy**
0.5%	**557**	30	0	0	0	94.89%
1.5%	245	**337**	5	0	0	57.41%
4%	45	79	**448**	15	0	76.32%
7%	11	22	145	**382**	27	65.08%
12%	1	11	38	139	**398**	67.80%
Average						**72.30%**
	c					
	0.5%	1.5%	4%	7%	12%	Accuracy
0.5%	**585**	2	0	0	0	99.66%
1.5%	66	**521**	0	0	0	88.76%
4%	1	29	**557**	0	0	94.89%
7%	0	1	49	**537**	0	91.48%
12%	0	0	1	37	**549**	93.53%
Average						**93.66%**
	SSIM					
	0.5%	1.5%	4%	7%	12%	**Accuracy**
0.5%	**584**	3	0	0	0	99.49%
1.5%	125	**462**	0	0	0	78.71%
4%	14	41	**532**	0	0	90.63%
7%	1	12	78	**496**	1	84.50%
12%	0	0	16	80	**491**	83.36%
Average						**87.39%**
	ΔH					
	0.5%	1.5%	4%	7%	12%	**Accuracy**
0.5%	**408**	160	19	0	0	69.51%
1.5%	214	**296**	77	0	0	50.43%
4%	46	101	**409**	31	0	69.68%
7%	2	8	95	**470**	12	80.07%
12%	0	1	3	53	**530**	90.29%
Average						**71.99%**

TABLE V
CONFUSION MATRIX OF DECEPTIVE JAMMING EVALUATION RESULTS WITH VOTING WEIGHTS OF DOMINANT INDICATORS

	0.5%	1.5%	4%	7%	12%	Rejected	**Accuracy**
0.5%	**574**	9	0	0	0	4	97.79%
1.5%	167	**402**	0	0	0	18	68.48%
4%	17	20	**518**	3	0	29	88.25%
7%	1	2	79	**471**	2	32	80.24%
12%	0	0	3	58	**479**	47	81.10%
Average							**70.73%**

TABLE VI
CONFUSION MATRIX OF DECEPTIVE JAMMING EVALUATION RESULTS WITH MULTILAYER PERCEPTRON WEIGHTS OF DOMINANT INDICATORS

	0.5%	1.5%	4%	7%	12%	**Accuracy**
0.5%	**187**	158	161	77	4	31.86%
1.5%	177	**162**	160	83	5	27.60%
4%	122	156	**152**	145	12	25.89%
7%	25	48	103	**339**	72	57.75%
12%	0	0	0	57	**530**	90.29%
Average						**46.68%**

TABLE VII
CONFUSION MATRIX OF DECEPTIVE JAMMING EVALUATION RESULTS WITH CNN

	0.5%	1.5%	4%	7%	12%	**Accuracy**
0.5%	**322**	261	4	0	0	54.86%
1.5%	79	**477**	31	0	0	81.26%
4%	0	16	**563**	8	0	95.91%
7%	0	0	3	**583**	0	99.32%
12%	1	0	1	7	**578**	98.47%
Average						**85.96%**

TABLE VIII
CONFUSION MATRIX OF DECEPTIVE JAMMING EVALUATION RESULTS WITH THE PROPOSED METHOD

	0.5%	1.5%	4%	7%	12%	**Accuracy**
0.5%	**521**	66	0	0	0	88.76%
1.5%	39	**540**	7	1	0	91.99%
4%	0	3	**581**	3	0	98.98%
7%	0	0	1	**585**	1	99.66%
12%	0	0	0	1	**586**	99.83%
Average						**95.84%**

Table VI lists the test results from the use of the neural network model with a multilayer perceptron to directly determine the weight. The average accuracy of the image deceptive evaluation is very low, since these dominant factors cannot fully represent the features of deceptive images. The net weight is greatly influenced by certain dominant evaluation factors with poor performance.

The performance evaluation accuracy using the CNN directly is only about 85.96%, due to low $R_s(t_m)$ measurement error. As the $R_s(t_m)$ measurement error increases, the accuracy approaches 100%, as shown in Table VII. The features extracted by CNN have no clear physical meaning, and cannot provide reliable support for expert judgment in a human–machine interface. Therefore, we apply the indicators extracted by the CNN as the recessive features. The performance evaluation accuracy using the proposed method is presented in Table VIII, which confirms that the proposed approach outperforms other comparison benchmarks. Its evaluation accuracy is less affected by the $R_s(t_m)$ measurement error.

Fig. 12 illustrated the comparison between the convergence curves of the CNN and the proposed method. The solid and dotted lines represent the convergence curves of the training and testing accuracy, respectively, with the CNN directly. The dotted and dash-dot lines represent the convergence curves of the training and testing accuracy, respectively, with the proposed method. From Fig. 12, it can be seen that the training accuracy reached a stable value after 150 epochs using the two methods.

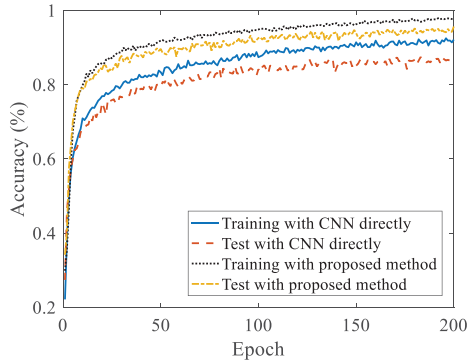

Fig. 12. Comparison of convergence of CNN directly and with proposed method.

The proposed method reached a training accuracy of 97.92% and a testing accuracy of 95.84%, outperforming using the CNN directly. This demonstrates the effectiveness of the proposed method.

V. CONCLUSION

To solve the issues of poor generalization ability and low adaptive processing efficiency of the PEoDJ methods, this article proposed a performance evaluation method that combines dominant and recessive features. The proposed method exhibits high evaluation accuracy and strong generalization ability, and supports the closed-loop working system of intelligent ECM. We analyzed the influence of the motion parameter measurement error of SAR on deceptive jamming images, and generated a large number of deceptive jamming images at different levels, which solves the problem of insufficient jamming samples. The proposed method was then verified on the MSTAR dataset. The experimental results demonstrated that the proposed method exhibits higher evaluation accuracy than other methods, which in turn indicates its effectiveness, robustness, and generalization performance.

REFERENCES

[1] A. Moreira, P. Prats-Iraola, M. Younis, G. Krieger, I. Hajnsek, and K. P. Papathanassiou, "A tutorial on synthetic aperture radar," *IEEE Geosci. Remote Sens. Mag.*, vol. 1, no. 1, pp. 6–43, Mar. 2013.

[2] D. Adamy, *Introduction to EW Modeling and Simulation*. Norwood, MA, USA: Artech House, 2003.

[3] Y. Huang, L. Zhang, J. Li, Z. Chen, and X. Yang, "Reweighted tensor factorization method for SAR narrowband and wideband interference mitigation using smoothing multiview tensor model," *IEEE Trans. Geosci. Remote Sens.*, vol. 58, no. 5, pp. 3298–3313, May 2020.

[4] F. Zhou, B. Zhao, M. Tao, X. Bai, B. Chen, and G. Sun, "A large scene deceptive jamming method for space-borne SAR," *IEEE Trans. Geosci. Remote Sens.*, vol. 51, no. 8, pp. 4486–4495, Aug. 2013.

[5] B. Zhao, L. Huang, F. Zhou, and J. Zhang, "Performance improvement of deception jamming against SAR based on minimum condition number," *IEEE J. Sel. Top. Appl. Earth Observ.*, vol. 10, no. 3, pp. 1039–1055, Mar. 2017.

[6] B. Zhao, F. Zhou, and Z. Bao, "Deception jamming for squint SAR based on multiple receivers," *IEEE J. Sel. Top. Appl. Earth Observ.*, vol. 8, no. 8, pp. 3988–3998, Aug. 2015.

[7] B. Zhao, L. Huang, J. Li, M. Liu, and J. Wang, "Deceptive SAR jamming based on 1-bit sampling and time-varying thresholds," *IEEE J. Sel. Topics Appl. Earth Observ.*, vol. 11, no. 3, pp. 939–950, Mar. 2018.

[8] Y. Liu, C. Wang, X. Pan, Q. Fu, and G. Wang, "Inverse omega-K algorithm for the electromagnetic deception of synthetic aperture radar," *IEEE J. Sel. Topics Appl. Earth Observ.*, vol. 9, no. 7, pp. 3037–3049, Jul. 2016.
[9] M. Osborne, *An Introduction to Game Theory*. New York, NY, USA: Oxford Univ. Press, 2003.
[10] X. Lin, P. A. Beling, and R. Cogill, "Multiagent inverse reinforcement learning for two-person zero-sum games," *IEEE Trans. Games*, vol. 10, no. 1, pp. 56–68, Jan. 2018.
[11] D. Bachmann *et al.*, "Games between jammers and radars," in *Proc. AOC Int. Symp.*, Feb. 2006, pp. 13–14.
[12] K. Li, B. Jiu, and H. Li, "Game theoretic strategies design for monostatic radar and jammer based on mutual information," *IEEE Access*, vol. 7, pp. 72257–72266, Jun. 2019.
[13] S. Haykin, "Cognitive radar: A way of the future," *IEEE Signal Process. Mag.*, vol. 23, no. 1, pp. 30–40, Jan. 2006.
[14] S. Noh and U. Jeong, "Intelligent command and control agent in electronic warfare settings," *Int. J. Intell. Syst.*, vol. 25, no. 6, pp. 514–528, Jun. 2010.
[15] Z. Liu and K. Xu, "The effectiveness index of SAR jamming based on information loss of images," *Acta. Electronica Sinica*, vol. 35, no. 6, pp. 1042–1045, 2007.
[16] X. Li and J. Zhen, "Information theory-based amendments of SAR jamming effect evaluation," in *Proc. Int. Symp. 6th Int. Conf. Internet Comput. Sci. Eng.*, Apr. 2012, pp. 159–162.
[17] F. Zhao, Y. Hu, and X. Tao, "Research on the effect evaluation based on information theory in imaging systems," *Laser Infrared*, vol. 38, no. 4, pp. 371–374, Apr. 2008.
[18] J. Shi, D. Bi, and L. Xue, "Novel evaluation method of jamming effect on ISAR based on target detection," in *Proc. 2nd Asian Pacific Conf. Synthetic Aperture Radar*, Oct. 2009, pp. 892–895.
[19] H. Zhao, "Simulation of barrage-type jamming for synthetic aperture radars," in *Proc. Int. Colloq. Comput., Commun., Control, Manage.*, Aug. 2008, pp. 462–465.
[20] B. Zhonggan, D. Xingsong, Z. Lei, and H. Letian, "Centroid-track based method for SAR jamming effect evaluation," in *Proc. IEEE Int. Conf. Electron. Meas. Instrum.*, Oct. 2017, pp. 406–410.
[21] X. Wu, D. Dai, X. Wang, and H. Lu, "Evaluation of SAR jamming performance," in *Proc. Int. Symp. MAPE*, Dec. 2007, pp. 1476–1480.
[22] M. Ammar, H. Hassan, M. Abdel-Latif, and S. A. Elgamel, "Performance evaluation of SAR in presence of multiplicative noise jamming," in *Proc. 34th Nat. Radio Sci. Conf.*, Mar. 2017, pp. 213–220.
[23] W. G. Carrara, R. S. Goodman, and R. M. Majewski, *Spotlight Synthetic Aperture radar: Signal Processing Algorithms*. Norwood, MA, USA: Artech House, 1995.
[24] X. F. Wu, D. Dai, and X. Wang, "Study on SAR jamming measures," in *Proc. IET Int. Radar Conf.*, Oct. 2007, pp. 1–5.
[25] B. Tang *et al.*, "A new method for evaluation of jamming effect on ISAR," in *Proc. 2nd Asian Pacific Conf. Synthetic Aperture Radar*, Oct. 2009, pp. 531–534.
[26] L. Sun, *et al.*, "Research on deceptive jamming technologies against SAR," in *Proc. 2nd Asian Pacific Conf. Synthetic Aperture Radar*, Oct. 2009, pp. 521–525.
[27] Y. Li and H. Chen, "Evaluation method of jamming effect on ISAR based on correlation coefficient," *J. Univ. Electron. Sci. Technol. China*, vol. 35, no. 4, pp. 468–470, Aug. 2006.
[28] W. Wang and G. Wang, "Minimum entropy based registration strategy for airborne SAR images before and after jamming," *Electron. Opt. Control*, vol. 15, no. 6, pp. 58–62, 2008.
[29] R. Cui and L. Xue, "Evaluation method of jamming effect on ISAR based on image entropy," *Mod. Def. Technol.*, vol. 37, no. 1, pp. 94–97, Feb. 2009.
[30] G. Han *et al.*, "Evaluation of jamming effect on SAR based on method of modified structural similarity," *J. Comput. Electron.*, vol. 33, no. 3, pp. 711–716, Mar. 2011.
[31] Z. Wang, A. Bovik, H. Sheikh, and E. P. Simoncelli, "Image quality assessment from error visibility to structure similarity," *IEEE Trans. Image Process.*, vol. 13, no. 4, pp. 600–612, Apr. 2004.
[32] F. Qin *et al.*, "Radar jamming effect evaluation based on AdaBoost combined classification model," in *Proc. IEEE 4th Int. Conf. Softw. Eng. Service Sci.*, 2013, pp. 910–913.
[33] S. Peng, *et al.*, "Study on quantitative efficiency evaluation for deception jamming to ISAR," in *Proc. 2nd Asian Pacific Conf. Synthetic Aperture Radar*, Oct. 2009, pp. 544–547.
[34] I. Goodfellow, Y. Bengio, and A. Courville, *Deep Learning*. Cambridge, MA, USA: MIT Press, 2016.
[35] G. Hinton *et al.*, "Deep neural networks for acoustic modeling in speech recognition: The shared views of four research groups," *IEEE Signal Process. Mag.*, vol. 29, no. 6, pp. 82–97, Nov. 2012.
[36] A. Krizhevsky, I. Sutskever, and E. Hinton, "ImageNet classification with deep convolutional neural networks," *Commun. ACM*, vol. 60, no. 6, pp. 84–90, Jun. 2017.
[37] S. Ji, W. Xu, M. Yang, and K. Yu, "3D convolutional neural networks for human action recognition," *IEEE Trans. Pattern Anal. Mach. Intell.*, vol. 35, no. 1, pp. 221–231, Jan. 2013.
[38] Y. Liu, W. Wang, X. Pan, L. Xu, and G. Wang, "Influence of estimate errors of radar kinematic parameters on deceptive jamming against SAR," *IEEE Sens. J.*, vol. 16, no. 15, pp. 5904–5911, Aug. 2016.
[39] K. Simonyan and A. Zisserman, "Very deep convolutional networks for large-scale image recognition," in *Proc. Int. Symp. ICLR*, May. 2015, pp. 1–14.
[40] L. N. Smith and N. Topin, "Deep convolutional neural network design patterns," in *Proc. Int. Symp. ICLR*, Apr. 2017, pp. 1–13.
[41] F. Rosenblatt, "A probabilistic model for visual perception," *Acta Cytol.*, vol. 15, pp. 296–297, 1959.
[42] O. Ciftcioglu, M. S. Bittermann, and I. S. Sariyildiz, "Towards computer-based perception by modeling visual perception: A probabilistic theory," in *Proc. IEEE Int. Conf. Syst., Man Cybern.*, Nov. 2006, pp. 5152–5159.

Tian Tian was born in Shaanxi, China, in 1992. She received the B.S. degree in electronic science and technology and Ph.D. degree in signal and information processing from Xidian University, Xi'an, China, in 2014 and 2020, respectively.

She is currently a Lecturer with the Ministry Key Laboratory of Electronic Information Countermeasure and Simulation, Xidian University. Her research interests include signal processing, radar imaging, and SAR countermeasure.

Feng Zhou (Member, IEEE) was born in Henan, China, in 1980. He received the M.S and Ph.D. degrees in signal and information processing from Xidian University, Xi'an, China, in 2004 and 2007, respectively.

He is currently a Professor and the Director of the Ministry Key Laboratory of Electronic Information Countermeasure and Simulation, Xidian University. His research interests include radar imaging and jamming suppression.

Prof. Zhou was granted the program for New Century Excellent Talents in University in China and was the recipient of the Young Scientist Award from XXXI URSI GASS Committee.

Yuchen Li was born in Jinzhou, China, in 1994. He received the B.S. degree in electrical information engineering from University of Electronic Science and Technology of China, Chengdu, China, in 2016, and the M.S. degree in signal and information processing from Xidian University, Shaanxi, China, in 2019.

His research interests include machine learning.

Bin Sun was born in Liaoning, China, in 1985. He received the M.S and Ph.D. degrees in information and communication engineering from National University of Defence Technology, Changsha, China, in 2012 and 2016, respectively.

He is currently an Assistant Research Fellow with Jinzhou Test Research Center, China. His research interests include radar signal processing and performance evaluation.

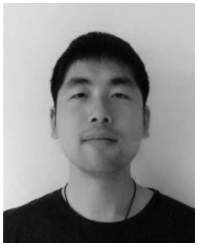

Weiwei Fan was born in Shanxi, China, in 1991. He received the B.S. degree in information countermeasure techniques and Ph.D. degree in signal and information processing from Xidian University, Xi'an, China, in 2014 and 2019, respectively.

He is currently a Lecturer with the Ministry Key Laboratory of Electronic Information Countermeasure and Simulation, Xidian University. His research interests include target detection, radar imaging, interference mitigation, and PolSAR.

Chen Gong (Senior Member, IEEE) received the B.S. degree in electrical engineering and mathematics (minor) from Shanghai Jiaotong University, Shanghai, China, in 2005, the M.S. degree in electrical engineering from Tsinghua University, Beijing, China, in 2008, and the Ph.D. degree in electrical engineering from Columbia University, New York City, NY, USA, in 2012.

He was a Senior Systems Engineer with the Qualcomm Research, San Diego, CA, USA, from 2012 to 2013. He is currently a Faculty Member with the University of Science and Technology of China. His research interests include wireless communications, optical wireless communications, and signal processing.

Dr. Gong received Hongkong Qiushi Outstanding Young Researcher Award, in 2016.

Shuang Yang was born in Shandong, China, in 1994. She received the M.S. degree in information and communications engineering from Xidian University, Xi'an, China, in 2020.

Her major research interests include radar image classification and target detection.